



Research paper

MagTFs: A tool for estimating multiple magnetic transfer functions to constrain Earth's electrical conductivity structure

Zhengyong Ren^a, Zijun Zuo^a, Hongbo Yao^{a,b,*}, Chaojian Chen^{a,**}, Linan Xu^c, Jingtian Tang^a, Keke Zhang^b

^a School of Geosciences and Info-Physics, Central South University, Changsha, 410083, Hunan, China

^b Macau Institute of Space Technology and Application, Macau University of Science and Technology, 999078, Macao Special Administrative Region of China

^c Institute of Earth Sciences, University of Lausanne, 1015 Lausanne, Switzerland

ARTICLE INFO

Dataset link: https://imag-data.bgs.ac.uk/GIN_V1/GINForms2, <https://earth.esa.int/eogateway/missions/swarm/data>

Keywords:

Electromagnetic induction
Transfer functions
Mantle electrical conductivity
Geomagnetic data
Ionospheric and magnetospheric sources

ABSTRACT

Time-varying magnetic signals measured by geomagnetic observatories and satellites carry information about the Earth's deep electrical conductivity structure and external current sources in the ionosphere and magnetosphere. Estimating magnetic transfer functions (TFs), which reflect the Earth's internal conductivity structure, is a primary task in interpreting geomagnetic data from observatories and satellites. However, available TFs estimation tools either focus on a single source (ionosphere currents or magnetosphere currents) or are not publicly accessible. Therefore, we developed a flexible TFs estimation tool, named MagTFs, to achieve robust and precise estimation of magnetic TFs from the time series of magnetic field data acquired through land or satellite-based observations. This tool can handle magnetic data originating from time-varying currents in both the ionosphere and magnetosphere. We tested its performance on four kinds of data sets, and the good agreements with published results underscore the tool's maturity and versatility in accurately estimating multi-source TFs. As a contribution to the scientific community, we have released MagTFs as an open-source tool, facilitating broader utilization and collaborative advancements.

1. Introduction

Understanding the Earth's electrical conductivity structure is essential for insights into its thermal-chemical conditions, as conductivity is sensitive to water and the presence of partial melt (Karato and Wang, 2013; Yoshino and Katsura, 2013). Geoelectromagnetic (EM) induction sounding techniques, such as the magnetotelluric (MT) method and the geomagnetic depth sounding (GDS) technique, are widely used to investigate this structure from the crust to the mantle (Chave and Jones, 2012; Kelbert et al., 2009; Kuvshinov, 2012; Li et al., 2020; Zhang et al., 2023; Yao et al., 2023a; Chen et al., 2023; Grayver, 2024). The MT method uses electromagnetic signals from the ionosphere to image conductivity structures down to the upper mantle, while the GDS technique can explore deeper structures down to the lower mantle by analyzing magnetic signals from the magnetosphere.

To reveal the Earth's conductivity structure, the first and crucial step for both methods is to estimate high-quality TFs from electromagnetic time series obtained on land, at the ocean floor, or through satellite data, which are then inverted to constrain the Earth's conductivity. The

precision of this estimation directly impacts the reliability of the imaging of the Earth's conductivity structure. Thus, accurately estimating TFs is essential for probing the Earth's conductivity structure.

Three types of electromagnetic data sets are measured to estimate EM TFs, as outlined in Table 1: (1) **MT Data**: Measured on a regional to continental scale, these data include both electric and magnetic fields. It enables the estimation of MT TFs, such as MT impedance or MT tipper, originating from the ionosphere, particularly for signals with periods less than 3 h (Chave and Jones, 2012). (2) **Magnetic Field Data from Global Geomagnetic Observatories**: These data facilitate the estimation of MT tipper and solar quiet (Sq) global-to-local TFs, covering periods ranging from several hours to one day and originating from the ionosphere (Guzavina et al., 2019). (3) **Magnetic Field Data from Geomagnetic Satellites**: These data can be used to estimate the GDS scalar C-response (Banks, 1969) and the matrix Q-response (Q-matrix) (Püthe et al., 2015). In this study, our emphasis is on estimating TFs using magnetic field measured from both geomagnetic

* Corresponding author at: Macau Institute of Space Technology and Application, Macau University of Science and Technology, 999078, Macao Special Administrative Region of China.

** Corresponding author.

E-mail addresses: hbyao@must.edu.mo (H. Yao), chenchaojian@csu.edu.cn (C. Chen).

<https://doi.org/10.1016/j.cageo.2024.105769>

Received 15 August 2024; Received in revised form 5 November 2024; Accepted 6 November 2024

Available online 19 November 2024

0098-3004/© 2024 Elsevier Ltd. All rights are reserved, including those for text and data mining, AI training, and similar technologies.

Table 1
List of different kinds of EM TFs.

Type of TFs	Period	Origin	Type of observations
Impedance	≤ 3 h	Ionosphere	MT
Induction vector	≤ 3 h	Ionosphere	MT, observatory
Sq G2L TFs	4 - 24 h	Ionosphere	MT, observatory
Dst G2L TFs	≥ 1 day	Magnetosphere	Observatory, satellite
C-response	≥ 1 day	Magnetosphere	Observatory, satellite
Q-matrix	≥ 1 day	Magnetosphere	Satellite

observatories and satellites. Notably, we exclude TFs using the electric field such as the MT impedance.

Several tools are available for estimating magnetic TFs using magnetic field measurements obtained from both geomagnetic observatories and satellites. A notable tool, developed by Olsen (1998), employs an algorithm to estimate the GDS C-response proposed by Banks (1969). This algorithm utilizes a section-averaging approach and iteratively re-weighted least squares. This method has been widely used in GDS studies (Olsen, 1999b; Semenov and Kuvshinov, 2012; Munch et al., 2018; Chen et al., 2020; Yao et al., 2023b, among others) and has been proven effective. Building on the conventional univariate processing code developed by Olsen (1998) and Püthe (2015) created a multivariate processing code capable of estimating TFs of scalar and arrays from various types of EM data. This tool, widely used in the estimation of MT tippers from observatory magnetic data (Morschhauser et al., 2019; Rigaud et al., 2021; Li et al., 2023, among others), has been expanded to estimate arrays of TFs linking the magnetic field to a set of spherical harmonic coefficients. This approach addresses the complex spatial structure of the magnetospheric source (Püthe et al., 2015). Furthermore, it has been extended to estimate the Sq global-to-local TFs, considering the intricate spatial structure of the ionospheric origin (Guzavina et al., 2019; Munch et al., 2020; Chen et al., 2023). Another well-known software, BIRRP, developed by Chave and Thomson (2003), is based on a bounded influence, remote reference method, aiming to estimate both the MT response and the GDS C-response. BIRRP has been extensively used in MT exploration (Baba et al., 2006; Fuentes-Arreazola et al., 2021; Gresse et al., 2021) and GDS imaging (Yuan et al., 2020; Zhang et al., 2020; Li et al., 2020). However, it should be noted that the above mentioned tools either focus on estimating magnetic TFs from a single source or are not publicly accessible.

In recent years, a significant number of new global public geomagnetic observatories have been established, complemented by non-public observatories dedicated to seismic monitoring and a substantial increase in MT data with periods approaching 10,000 s, as evidenced by the USArray and SinoProbe projects (Zhao et al., 2022; Murphy et al., 2021; Shao et al., 2024). Additionally, the deployment of geomagnetic satellites, such as ESA's Swarm, Macau Science Satellite-1, and the forthcoming NanoMagSat Constellation - New ESA Scout (Wood et al., 2022; Yan and Yao, 2024; Arranz et al., 2023), continues to enrich the data pool available to the geophysical community. Despite these advancements, a major bottleneck in the interpretation of geomagnetic induction data is the absence of a reliable and standardized open-source data processing tool. The growing complexity and volume of these datasets underscore the necessity for a comprehensive solution that is accessible to researchers worldwide. Currently, the lack of such a tool significantly impedes the efficient and accurate processing and interpretation of data, which is critical for imaging the thermal state and structure of the Earth's interior.

To address these challenges, an effective tool must encompass several key features:

- 1. Robust Performance:** The software must efficiently handle large datasets, including long-period MT data and geomagnetic satellite data, which require robust algorithms and considerable computational resources.

- 2. Accuracy and Reliability:** The software must produce precise and dependable TFs, essential for the interpretation of geomagnetic induction data. This requires rigorous testing and validation against established benchmarks and datasets.
- 3. Accessibility and Open Source:** To maximize its utility, the software should be open source, enabling researchers to freely access, modify, and enhance the code. This fosters a collaborative development environment and ensures the tool remains current with the latest advancements in the field.
- 4. Extensibility:** The software should be designed with extensibility in mind, allowing for the addition of new features and functionalities as research needs evolve and new data processing techniques emerge.

In response to these needs, we have developed an open-source tool for estimating multisource magnetic TFs from signals measured at observatories or by satellites. It can also be extended to process MT data, though adjustments are required to accommodate the MT data acquisition format, as the sampling rates vary across different MT frequency bands. This tool utilizes a robust, section-averaged linear regression scheme, inspired by the work of Olsen (1998) and Püthe et al. (2015). Its novelty lies in its ability to estimate magnetic TFs using signals from both the ionosphere and magnetosphere when measured at observatories, and from the magnetosphere when obtained from satellites. To validate the efficacy of the tool, we conducted four case studies. In each case, we estimated the TFs from various sources and compared them with previously published results. Additionally, parameter studies were performed to investigate the influence of different parameters on the estimated TFs. These rigorous assessments confirm the accuracy and reliability of our open-source tool, establishing its utility for estimating magnetic TFs from diverse electromagnetic signal sources.

2. Method

Geomagnetic observatory and satellite data are the two main data sources for constraining Earth's mantle conductivity structures. Geomagnetic observatories measure magnetic data at fixed locations and have a good local resolution beneath the observatories, but lack resolution in oceanic regions. Compared to geomagnetic observatories, geomagnetic satellites can measure globally covered magnetic data, but with complex spatial-temporal variability. Meanwhile, for both observatories and satellites, the measured time-varying magnetic data include the contributions from ionospheric and magnetospheric current sources. Here, we describe the definition and the estimation of multisource magnetic TFs from geomagnetic observatory and satellite data and our open-source code implementation.

2.1. Multi-source magnetic TFs

2.1.1. MT tipper

The variations in the geomagnetic field with periods less than 3 h mainly originate from the auroral ionospheric current. This current system allows us to establish a relationship between the vertical magnetic field component, Z , and the horizontal magnetic field, $H_r = (H_x, H_y)$, using the MT tipper, $T = (T_{xy}, T_{zy})$ (Berdichevsky and Dmitriev, 2008):

$$Z(\mathbf{r}_s, \omega) = T_{zx}(\mathbf{r}_s, \omega)H_x(\mathbf{r}_s, \omega) + T_{zy}(\mathbf{r}_s, \omega)H_y(\mathbf{r}_s, \omega). \quad (1)$$

Here, \mathbf{r}_s represents the coordinates of an observation site, $\omega = 2\pi/T$ denotes the angular frequency, and T is the period.

2.1.2. Ionospheric Sq global-to-local TFs

The daily Sq variations, with periods ranging from a few hours to 24 h, mainly originate from the mid-latitude ionospheric current

system, which has a complex spatiotemporal structure (Yamazaki and Maute, 2017; Guzavina et al., 2019). Conventionally, the local C-response concept, which represents the source using a single spherical harmonic (SH) specific to each Sq frequency period (will be described later), is adopted to analyze Sq variations (Schmucker, 1970; Bahr and Filloux, 1989; Schmucker, 1999a). However, it is too simplistic to use a single SH to describe the ionospheric source. To overcome this problem, Püthe et al. (2015) proposed the concept of global-to-local (G2L) TFs to account for the complex spatiotemporal structure of the Sq source. These G2L TFs, T_n^m , relate a set of SH expansion coefficients, ϵ_n^m , describing the source to a locally measured vertical magnetic field, Z , by Püthe et al. (2015) and Guzavina et al. (2019)

$$Z(\mathbf{r}_s, \omega_p) = \sum_{n,m \in L(\omega_p)} \epsilon_n^m(\omega_p) T_n^m(\mathbf{r}_s, \omega_p), \quad (2)$$

where the symbol $L(\omega_p)$ represents a set of SH for each Sq frequency ω_p , which corresponds to a period of $T_p = 24/p$ hours, with $p = 1, 2, 3, 4$. The summation in Eq. (2) reads

$$\sum_{n,m \in L(\omega_p)} = \sum_{m=p-1}^{p+1} \sum_{n=m}^{m+3}. \quad (3)$$

The definition of Sq G2L TFs in Eqs. (2)–(3) results in 11 SH terms for the period of 24 h and 12 SH terms for the periods of 12, 8, and 6 h.

2.1.3. Magnetospheric scalar C-response

Magnetic field variations in the period ranging from a few days to a few months mainly originate from the magnetospheric ring current. At the ground, the spatial structure of the large-scale magnetospheric ring current could be described via the first zonal spherical harmonic, Y_1^0 (Banks, 1969; Schultz and Larsen, 1987). Assuming this source geometry, one can determine the local C-response as (Banks, 1969)

$$C(\mathbf{r}_s, \omega) = -\frac{a \tan \theta}{2} \frac{B_r(\mathbf{r}_s, \omega)}{B_\theta(\mathbf{r}_s, \omega)}, \quad (4)$$

where a is the Earth's mean radius, θ is the geomagnetic colatitude of the geomagnetic observation site \mathbf{r}_s . $B_r = -Z$ and B_θ correspond to the respective radial and co-latitudinal magnetic field components.

Note that the local C-response concept in Eq. (4) is based on the assumption that the geometry of the magnetospheric ring current is simple, so it can be well approximated by Y_1^0 SH. However, more and more evidence demonstrates a more complex structure and asymmetry of the magnetospheric source (Balasis and Egbert, 2006; Luhr et al., 2017). To address this problem, one can use the global-to-local TFs described in Eq. (2), as illustrated in Püthe et al. (2015).

2.1.4. Magnetospheric Q-matrix

The local C-response described above is widely used in handling magnetic data measured at geomagnetic observatories (Kelbert et al., 2009; Semenov and Kuvshinov, 2012; Munch et al., 2018; Yao et al., 2022, among others). Another data source that can be used to analyze magnetic field variations of magnetospheric origin is satellite-borne measurements, for instance, *Swarm* (Olsen et al., 2013), CHAMP (Reigber et al., 2002), CryoSat-2 satellite (Olsen et al., 2020) and Macau Science Satellite-1 (Zhang, 2023). Working with satellite geomagnetic data, one cannot adopt the above-discussed local C-response or G2L TFs concepts. This is because the satellite moves constantly, causing spatio-temporal aliasing. An alternative magnetic TFs that can be used to process satellite geomagnetic data is the so-called Q-matrix, Q_{kn}^{lm} , which relates the inducing (external) ϵ_n^m and induced (internal) l_k^l SH coefficients (Olsen, 1999a; Püthe and Kuvshinov, 2014)

$$l_k^l(\omega) = \sum_{n=1}^{N_{\text{ext}}} \sum_{m=-n}^n Q_{kn}^{lm}(\omega) \epsilon_n^m(\omega), \quad (5)$$

where N_{ext} is the maximum cutoff degree describing the magnetospheric current source; Q-matrix is a 2-D array of TFs, which means that for a 3-D Earth model, each inducing coefficient generates an infinite series of induced coefficients. For a 1-D Earth model, each inducing

coefficient produces exactly one induced coefficient of the same degree and order, which can be related through the scalar Q-response:

$$l_n^m(\omega) = Q_n(\omega) \epsilon_n^m(\omega). \quad (6)$$

Here, Q_n is the so-called scalar Q-response, and is independent of the order m .

2.2. Estimation of magnetic TFs

Here, we take MT tipper as an example to illustrate the procedure for estimating TFs and the corresponding data standard errors from magnetic time series by MagTFs. The input signals are the time series of the horizontal magnetic fields $H_x(t)$ and $H_y(t)$, and the output signal is the time series of the vertical magnetic field $Z(t)$. Our method closely follows previous works (Olsen, 1998; Semenov and Kuvshinov, 2012; Püthe, 2015):

- (1) Cut the input and output time series of period T into N segments. Each segment has a length of KT with $3 \leq K \leq 12$. Adjacent segments may overlap, with overlap percentage c in the range $c = [0, 100\%)$. Then, the maximum period of TFs can be estimated by

$$T \leq \frac{L}{K[2 + (N-2)(1-c)]}, \quad (7)$$

with L being the length of the time series.

- (2) Multiply the time series of each segment with a window function, such as the Hamming window function, Blackman window function, Flat-top window function, and Triangular window function, to mitigate spectral leakage. The Hamming window is used in this study:

$$W(t) = a_0 - (1 - a_0) \cdot \cos\left(\frac{2\pi t}{N_t - 1}\right) \quad 0 \leq t \leq N_t - 1. \quad (8)$$

Here, $a_0 = 0.53836$, and N_t represents the number of samples in the segment.

- (3) Compute the spectra of the input and output signals. In this study, we perform a Fourier transform on each segment of the time series to obtain the frequency spectra $F(\omega)$ of the input and output signals $f(t)$:

$$F(\omega) = \int_{t_l}^{t_l + KT} f(t) W(t) e^{i\omega t} dt, \quad (9)$$

where $F(\omega)$ and $f(t)$ can be components of horizontal and vertical magnetic fields. l is a subscript representing the division of the input time series into N segments, each of which starts at the time when the input series is Fourier transformed.

- (4) Assemble a least-squares system. According to Eq. (1), each segment constitutes a linear equation, and all segments constitute a system of linear equations:

$$\begin{bmatrix} Z^{(1)}(\omega) \\ Z^{(2)}(\omega) \\ \vdots \\ Z^{(N)}(\omega) \end{bmatrix} = \begin{bmatrix} H_x^{(1)}(\omega) & H_y^{(1)}(\omega) \\ H_x^{(2)}(\omega) & H_y^{(2)}(\omega) \\ \vdots & \vdots \\ H_x^{(N)}(\omega) & H_y^{(N)}(\omega) \end{bmatrix} \begin{bmatrix} T_{zx}(\omega) \\ T_{zy}(\omega) \end{bmatrix}. \quad (10)$$

In matrix form, we have

$$\mathbf{Ax} = \mathbf{b}. \quad (11)$$

By solving the system of linear equations, we can obtain the corresponding responses.

- (5) Solve the linear system of equations in Eq. (11). To decrease the influence of outliers, we adopt the iteratively reweighted least squares (IRLS) method with Huber weights (Aster et al., 2018) to solve the system of linear equations:

$$\mathbf{x} = (\mathbf{A}^H \mathbf{W} \mathbf{A})^{-1} \mathbf{A}^H \mathbf{W} \mathbf{b}, \quad (12)$$

where the superscript H denotes the conjugate complex, and \mathbf{W} is a diagonal matrix representing Huber weights for each iteration (Sabaka et al., 2004).

- (6) Estimate data standard errors. During inversion, it is essential to assign data weights to each TFs using the data covariance matrix. Typically, the elements of the diagonal data covariance matrix are the squares of the inverse standard errors of the data. For the i th TFs, denoted as x_i , the jackknife data variance is calculated as (Chave and Thomson, 1989):

$$C_i = \frac{N-p}{N} \sum_{l=1}^N (\hat{x}_i^{(l)} - \bar{x}_i)^2, \quad (13)$$

where p is the number of channels of input signals ($p = 2$ for MT tipper), $\hat{x}_i^{(l)}$ represents the solution for least squares system with the l th segment being deleted, and \bar{x}_i is defined as:

$$\bar{x}_i = \frac{1}{N} \sum_{l=1}^N \hat{x}_i^{(l)}. \quad (14)$$

The standard errors of the data can be calculated by taking the square root of the variance of the data.

The procedures for estimating the Sq G2L TFs, magnetospheric scalar C-response, and magnetospheric Q-matrix is similar to the procedure mentioned above. The detailed procedures are given in Appendix A, B, and C.

2.3. Features of MagTFs

We have developed an open-source C++ tool, called MagTFs, which implements a procedure for estimating multi-source magnetic TFs. MagTFs offers various useful features for practical applications:

- Multi-source magnetic TFs estimation, including MT tipper, G2L TFs and scalar C-response from geomagnetic observatory data, and Q-matrix from geomagnetic satellite data.
- Parallel acceleration with OpenMP. MagTFs uses OpenMP to fast process very long time series of data with many segments.
- It can handle time series with discontinuity by cutting the input and output time series into multiple pieces. This feature is especially important for processing geomagnetic observatory data.
- It can estimate TFs with both logarithmic equally spaced periods and user-defined discrete periods.

The process of MagTFs is demonstrated in Fig. 1. The flowchart starts with the input of time series data. Following this, the estimation of the response and the calculation of the error are carried out using MagTFs, which comprises three primary modules:

- (1) Data pre-processing. It consists of three main steps: segmenting the time series, applying windowing in the time domain, and performing the Fourier transformation as described in Section 2.2.
- (2) Estimation of magnetic TFs. This module assembles segmented input and output signals, along with the desired TFs and residuals, into a set of equations. To solve this set of equations, the IRLS method is used.
- (3) Calculation of the standard deviation. This module is useful for weighting the observed data during inversion.

To facilitate the presentation and understanding of the algorithm, we have summarized the pseudocode for MagTFs as follows. It mainly includes average segmentation, window functions, Fourier transform, least-squares solution, estimation of geomagnetic response functions, and finally, the use of the Jackknife method to estimate data uncertainty.

Algorithm 1 Estimating Geomagnetic Transfer Functions.

Initialize parameters

Define input and output channels

Prepare variables for storing transfer functions (TF), uncertainties (delta_TF), and coherence squared (coh2)

for each period in n_periods do

Calculate segment length and Hamming window for data smoothing

for each piece of data do

for each segment in the data do

Step 1: Cut segments

Divide time series data into segments of length KT

Calculate maximum segment number and mark gaps

Step 2: Apply window function

Apply Hamming window to reduce spectral leakage

Step 3: Fourier transform

Perform Fourier Transform on the windowed data to obtain frequency-domain signals

if segment contains gaps then

Mark segment for exclusion

else

Assemble linear system matrices (A for input, b for output)

end if

end for

if segments are valid then

Step 4: Least-squares solution

Solve the least-squares linear system to estimate transfer functions using IRLS and Huber weight

Step 5: Estimate geomagnetic response functions

Calculate transfer functions and squared coherence for quality assessment

end if

end for

for each output channel do

Step 6: Estimate jackknife uncertainty

Perform jackknife resampling to estimate data uncertainty

Remove each segment once and solve the linear system for transfer function estimation

Calculate the variance of the transfer function for uncertainty estimation

end for

Output transfer functions, uncertainties, and coherence values to file

end for

3. Validation

To validate the performance of the developed MagTFs tool, we conducted four experiments on estimating the magnetic TFs originated from different sources. Specifically, we estimated the MT tipper, Sq G2L TFs, scalar C-response from observatory geomagnetic data and Q-matrix from satellite geomagnetic data. Geomagnetic observatory data are obtained from the International Real-Time Magnetic Observatory Network (INTERMAGNET) (Kerridge, 2001). Information about these data is given in Table 2. Swarm satellite data are taken from the European Space Agency (Olsen et al., 2013).

Throughout these experiments, we verified the precision of the magnetic TFs estimated by MagTFs by comparing them with the published results. Furthermore, we investigated the influence of different input parameters of MagTFs on the estimated TFs, including the window function, section overlap, and segment length. The aim of our analyses is to identify the optimal input parameters to improve the accuracy of the magnetic TFs estimation.

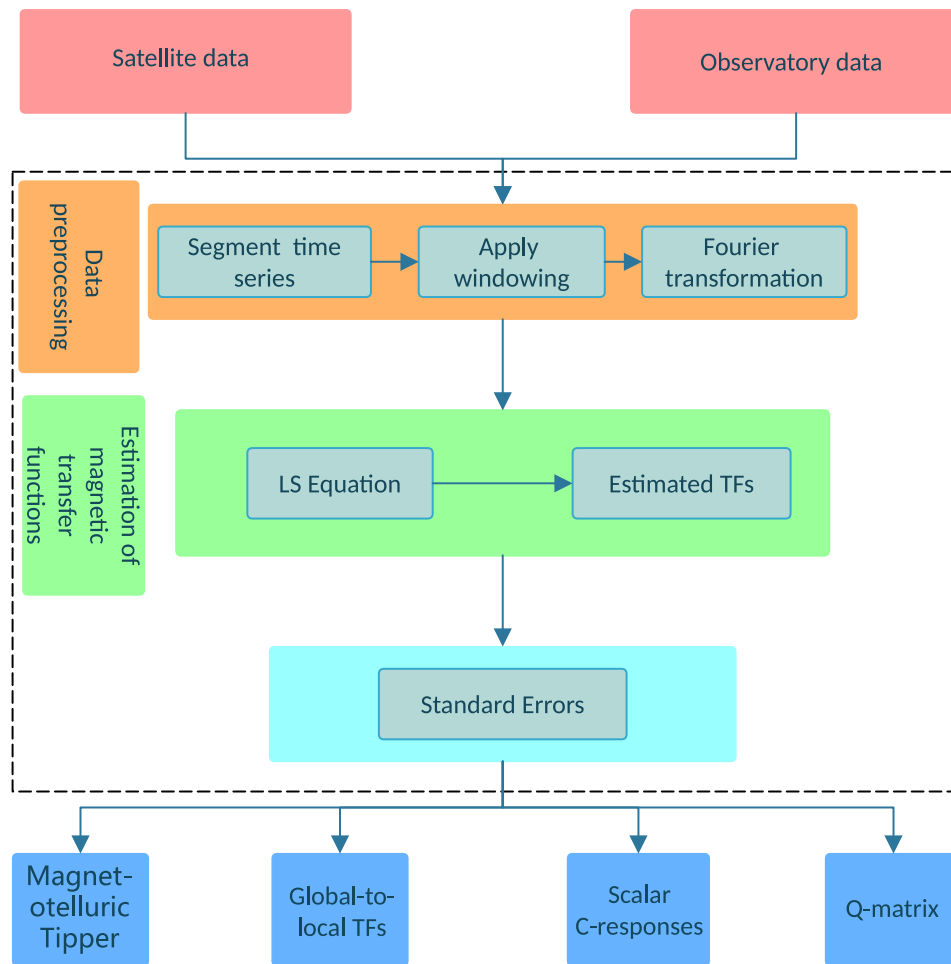


Fig. 1. Flowchart of MagTFs.

Table 2
Summary of geomagnetic observatories acronyms, names, geographic coordinates, and time interval of measured data.

Acronym	Name	latitude,longitude (deg)	Data length	TFs
CKI	Cocos-Keeling Islands	−12.19, 96.83	01/01/2017 - 31/12/2017	MT tipper
FRD	Fredericksburg	38.21, 282.63	01/01/1957 - 31/12/2007	C-responses
			11/09/1964 - 28/03/2010	Sq G2LTFs
ESA	Esashi	39.24, 141.35	04/03/1997 - 22/10/2016	Sq G2LTFs
BMT	Beijing Ming Tombs	40.3, 116.2	03/03/2000 - 29/10/2021	Sq G2LTFs
IRT	Irkutsk	52.27, 104.45	01/01/1957 - 31/12/2007	C-responses
			11/09/1964 - 18/10/2009	Sq G2LTFs
KAK	Kakioka	36.23, 140.18	01/01/1957 - 31/12/2007	C-responses
MMB	Memambetsu	43.91, 144.19	01/01/1957 - 31/12/2007	C-responses

3.1. Estimating MT tipper from observatory data

The first experiment aimed to determine the MT tipper using MagTFs, based on data collected from a geomagnetic observatory. The observatory chosen for this study was located at Cocos-Keeling Island in the Indian Ocean, with the INTERMAGNET code CKI. The results of [Rigaud et al. \(2021\)](#) used one-year minute-mean magnetic field data to estimate the MT tipper within a period range from 300 s to 8940 s. To ensure consistency and rigor with previous results, we used the one-year minute-mean magnetic field data measured at this observatory in 2017 to estimate the MT tipper within the same period range. We also estimated the tipper for the generally recognized period range (300 s to 10800 s), and the resulting trend was found to be consistent with the results for the period range of 300 s to 8940 s. For longer periods, we have fewer segments available, which affects the final response function estimates. Before estimating the MT tipper,

we identified noticeable spikes in the selected time series through a program and replaced the spike data with linear interpolation based on the surrounding data. Since the data quality at each point varied, they were processed individually and not included in the MagTFs software. Finally, the MT tippers and coherence were estimated in each period using MagTFs.

To demonstrate the precision of the MT tippers estimated by MagTFs, we compared with the results obtained by [Rigaud et al. \(2021\)](#) as depicted in [Fig. 2](#). Note that the estimated MT tippers by MagTFs shown in [Fig. 2](#) were obtained using the Hamming window function, section overlap of 50% and a segment length of 3. The impact of each parameter on the estimated MT tippers will be described later. It is also worth noting that [Rigaud et al. \(2021\)](#) also estimated MT tippers using the same CKI magnetic data from 2017 and employed the iteratively re-weighted least squares method introduced by [Olsen \(1998\)](#). As illustrated in [Fig. 2](#), there is a very good agreement between

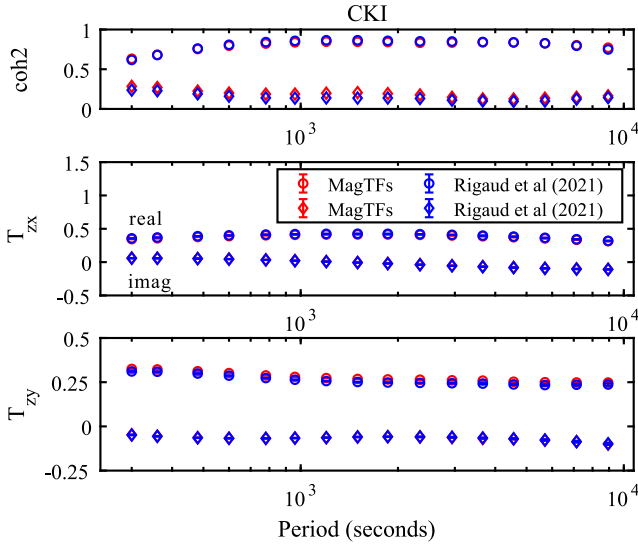


Fig. 2. Comparison of estimated MT tippers by MagTFs and Rigaud et al. (2021) at observatory CKI: the coherence (coh2), T_{zx} , and T_{zy} . Error bars represent the uncertainties.

the estimated T_{zx} and T_{zy} (both real and imaginary components) by MagTFs and those obtained by Rigaud et al. (2021). Additionally, the coherence of the estimated MT tippers demonstrates a significant overlap, thereby confirming the accuracy of the MT tippers estimated by MagTFs.

As described in Section 2.2, there are mainly three input parameters that may affect the estimation of TFs by MagTFs, including the window function, section overlap and segment length. Here, we performed a parameter study to investigate the impacts of different input parameters on the estimated TFs by MagTFs.

Regarding the influence of window function, four different types were selected: Hamming, Blackman, Flat-top, and Triangular. These window functions were chosen on the basis of their unique properties in spectral analysis. Fig. 3 shows the MT tippers estimated using these four window functions and the results obtained by Rigaud et al. (2021). Generally, the estimated MT tippers were consistent with those of Rigaud et al. (2021), particularly the results obtained from the Hamming window function. However, minor discrepancies were observed for long periods between the estimated TFs using Blackman, Flat-top, and Triangular window functions and those from Rigaud et al. (2021). Furthermore, the squared correlation coefficients of the estimated MT tippers using Blackman, Flat-top, and Triangular window functions exhibited a noticeable decline at long periods, probably due to the existing noise in time series. The Hamming window strikes a good balance between frequency resolution and noise reduction, making it especially suitable for analyzing magnetic TFs. These findings advocate for the use of the Hamming window function to improve the reliability of the estimated TFs. It is worth noting that additional experiments were conducted to investigate the effect of window function on estimating other magnetic TFs, which yielded similar results, but are not shown here.

We subsequently examine the influence of section overlap on the estimation of magnetic TFs. Here we analyze four distinct overlap ratios, specifically 30%, 50%, 70%, and 90%. In this experiment, the Hamming window function is used as suggested earlier. As illustrated in Fig. 4, the MT tipper (both real and imaginary components) computed with different section overlaps shows great agreement. Minor variations are noted in the long-period MT tipper estimates, but these differences fall within the experimental uncertainties. This suggests that the overlap ratio minimally affects the accuracy of the estimated MT tipper. However, higher overlap ratios substantially increase the

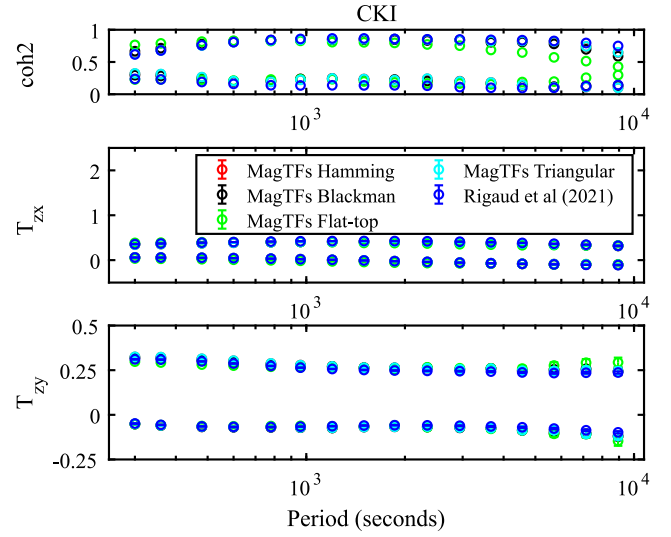


Fig. 3. Induction vector estimated with different window functions and their comparison with Rigaud et al. (2021) for the Cocos-Keeling Islands (CKI) observatory. Red, black, green, and cyan colors represent the Induction vector estimated by MagTFs when the window functions are Hamming, Blackman, Flat-top, and Triangular windows, respectively, and the blue MT tipper is from Rigaud et al. (2021). Error bars indicate uncertainty in the estimated Induction vector.

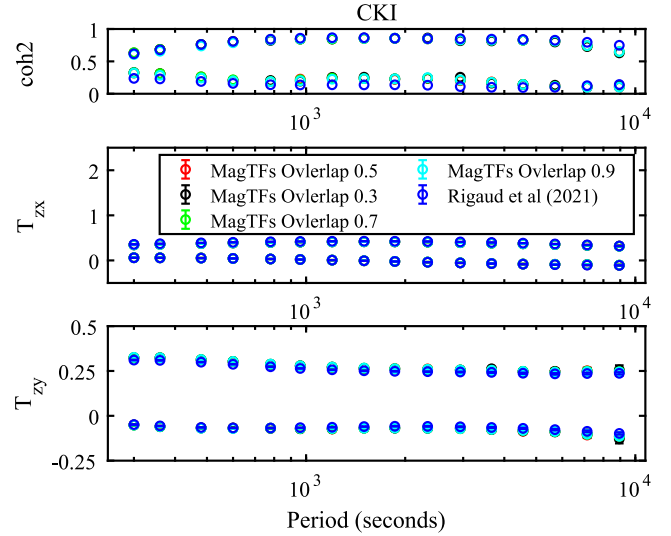


Fig. 4. Similar to Fig. 3, but for the results of using different section overlaps.

computational time. For a month's worth of observational data from the CKI observatory, the computational time for segment overlaps of 30%, 50%, 70%, and 90% were about 4 s, 8 s, 29 s, and 246 s, respectively. This rise is due to the increased volume of data processing required for higher overlaps. A 90% overlap, for example, necessitates more computational resources than 30% or 50% overlaps, leading to longer processing times and higher computational expenses.

Taking into account both efficiency and computational demands, this study recommends using a 50% overlap ratio. This ratio provides a balance that ensures adequate statistical reliability without incurring excessive computational time. Therefore, a 50% overlap ratio is suggested as an optimal choice for practical applications, offering an effective trade-off between accuracy and computational efficiency. The findings for the other TFs across the four different section overlaps mirrored the results discussed above, so they will not be reiterated here.

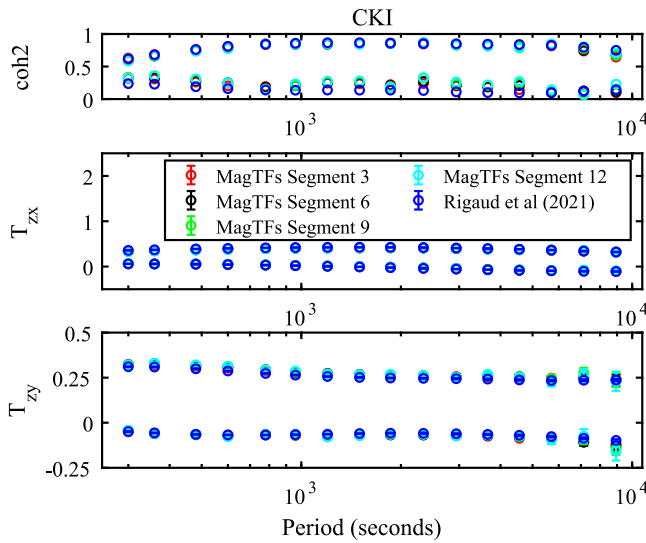


Fig. 5. Similar to Fig. 3, but for the results of using different segment lengths.

In our subsequent analysis, we examined how different segment lengths impact the estimated MT tipper. We specifically assessed segment lengths of 3, 6, 9, and 12 units, as presented in Fig. 5. It is clear that with a segment length of 12, the estimated results show some discrepancies compared to Rigaud et al. (2021), particularly in long-period estimates. However, in general, the results are in line with Rigaud et al. (2021). The impact of segment length on the estimation of other TFs differs from that in the MT tipper. For example, segment lengths of 3 or 6 are more effective in estimating C-responses from geomagnetic observatory data compared to segment lengths of 9 and 12. These details will be discussed further in Section 3.3. Based on these results, we recommend using segment lengths of 3 or 6 units for accurate estimation of magnetic TFs.

In our upcoming experiments aimed at estimating multi-source magnetic TFs, the Hamming window function will be employed, with a section overlap set to 50% and a segment length of 3, unless stated otherwise.

3.2. Estimating Sq G2L TFs from observatory data

In this experiment, we used the newly developed MagTFs tool to estimate the Sq G2L TFs originating from ionospheric geomagnetic signals. To estimate Sq G2L TFs at four different periods $T_p = 24/p$ hours (where $p = 1, 2, 3, 4$), geomagnetic data collected from four observatories (BMT in Beijing, ESA in Esashi, FRD in Fredericksburg, and IRT in Irkutsk) were used.

Estimation of Sq G2L TFs relies on the determination of external SH coefficients ϵ_n^m in Eq. (2) for each period. This is accomplished using an IRLS regression approach using global geomagnetic observatory data (Koch and Kuvshinov, 2013; Guzavina et al., 2019). Once the external SH coefficients ϵ_n^m are determined, MagTFs employs another IRLS regression to estimate the Sq G2L TFs T_n^m at the four observatories mentioned above.

Given that Sq G2L TFs of terms with $n = p + 1$ are dominant (Schmucker, 1999b), we only plot term T_{p+1}^p at periods ranging from 6 to 24 h using MagTFs and compared to those of Guzavina et al. (2019), as presented in Fig. 6. Since the coherence of the estimated Sq G2L TFs was not provided by Guzavina et al. (2019), we only present our results in Fig. 6. The Sq G2L TFs we estimated at four different observatories align well with the ones reported in Guzavina et al. (2019), indicating that MagTFs are effective in dealing with magnetic TFs of ionospheric origin that have a complex spatiotemporal structure.

The tidal magnetic signal has a similar period and is typically removed during the preprocessing of magnetic data at coastal observatories to mitigate its influence (Guzavina et al., 2018, 2019). As shown in Fig. 6, for the geomagnetic observatories considered here, correcting tidal magnetic signal has only a negligible effect on the estimated TFs. Therefore, we did not correct ocean tidal signals in this work. But for higher accuracy, we suggest correcting the tidal magnetic signal using the method of Guzavina et al. (2018, 2019).

3.3. Estimating scalar C-response from observatory data

To evaluate the capability of MagTFs in estimating magnetic TFs from geomagnetic data of magnetospheric origin, we calculated the local scalar C-response using observatory data. We utilized 51 years of geomagnetic data from four observatories located in the United States (FRD), Japan (KAK and MMB), and Russia (IRT). These observatories were selected to compute the local scalar C-response at periods from 2.96 days to 104.17 days. The specific locations of the observatories and the duration of data used in this experiment can be found in Table 2. Prior to estimation, we corrected for the Earth's core field and its secular variations. To validate the precision of the C-response estimated by MagTFs, we compared our results with those presented in Semenov and Kuvshinov (2012).

Fig. 7 shows a comparison between the C-response and coherence at four geomagnetic observatories by magTFs and Semenov and Kuvshinov (2012). The error bars represent the uncertainties in the estimated C-responses. The C-responses estimated by MagTFs align well with those estimated by Semenov and Kuvshinov (2012) within the uncertainties, with MagTFs having narrower error bars. However, the estimated C-response by MagTFs have smaller coherences at larger periods compared to those of Semenov and Kuvshinov (2012) (see Fig. 7(a) for MMB and Fig. 7(d) for IRT observatories). This might be due to the extensive efforts made by Semenov and Kuvshinov (2012) in terms of data selection, calibration, and denoising (refer to Semenov and Kuvshinov (2012) for more details). Nevertheless, this suggests that MagTFs is capable of effectively analyzing realistic observatory data and accurately estimating C-response.

As mentioned in Section 3.1, segment length – a key input parameter – significantly influences the estimated C-responses. Here we detail the effect of segment length on C-response estimation at MMB observatory. We estimated C-responses using four different segment lengths – 3, 6, 9, and 12 units – as illustrated in Fig. 8. Fig. 8 clearly shows that for longer C-response periods, segment lengths of 9 and 12 units lead to significant deviations from Semenov and Kuvshinov (2012). These deviations are manifested as larger error bars, indicating increased uncertainty and decreased reliability in long-period C-response estimates. Conversely, segment lengths of 3 and 6 units yield C-response estimates that align with Semenov and Kuvshinov (2012). These shorter segment lengths exhibit moderate error bars, reflecting a more stable and reliable estimation process. The stability provided by these segment lengths ensures the accuracy and consistency of the estimated C-response with Semenov and Kuvshinov (2012). Referring to Section 3.1's discussion on segment lengths affecting MT tipper estimation, we recommend using segment lengths of 3 or 6 units for precise magnetic TFs estimation.

3.4. Estimating Q-matrix from satellite data

The final experiment utilizes MagTFs to estimate the Q-matrix from geomagnetic satellite data originating in the magnetosphere. The input data consists of the time series of magnetospheric inducing and induced coefficients. These coefficients were obtained by Sabaka et al. (2018) through six years of Swarm satellite data (spanning from January 2013 to December 2018) and a comprehensive inversion technique. For further details on Q-matrix estimation, refer to Kuvshinov et al. (2021).

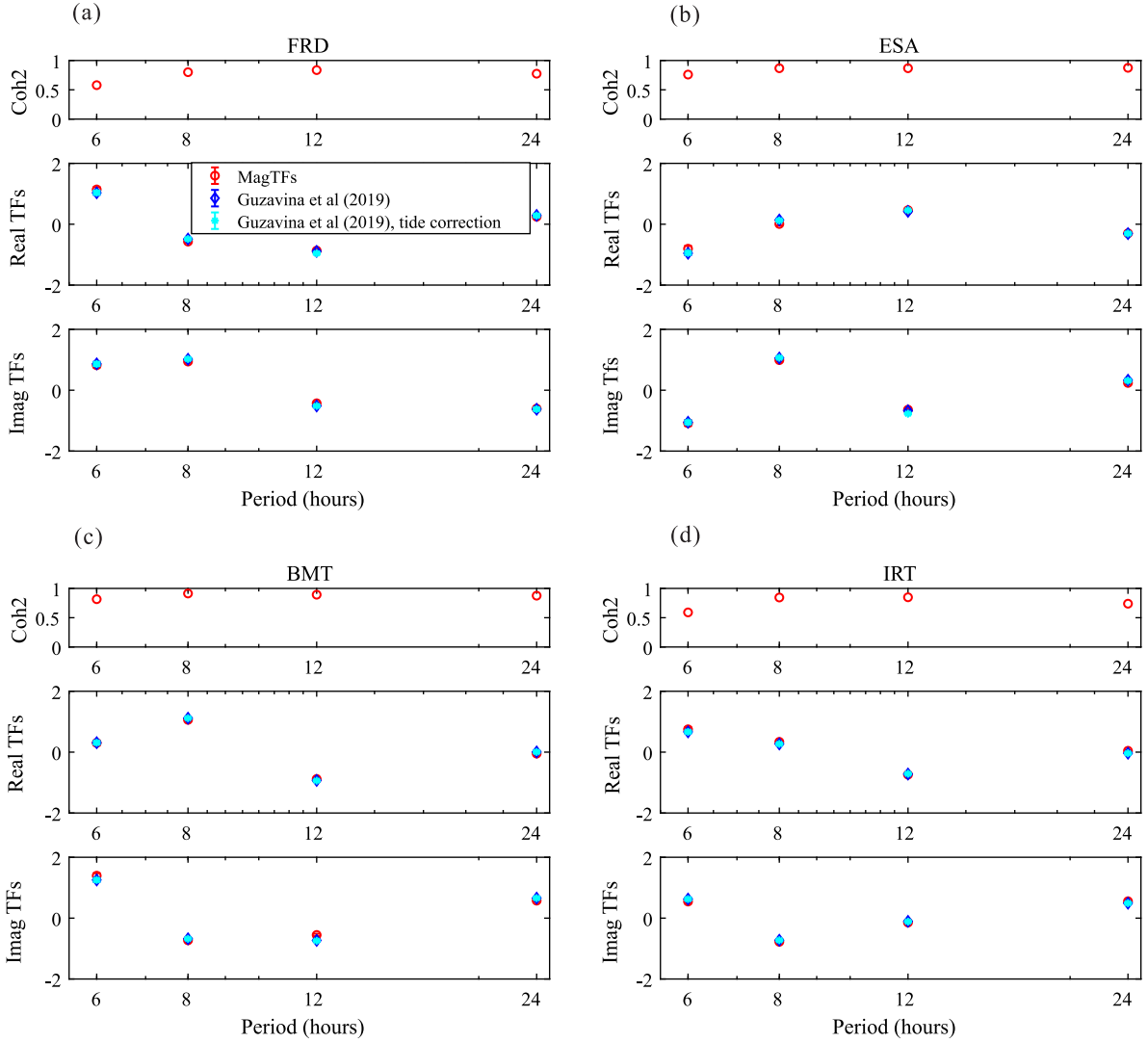


Fig. 6. Comparison of solar quiet global-to-local TFs of dominant term T_{p+1}^p , $p = 1, 2, 3, 4$ at four geomagnetic observatories: (a) FRD, (b) ESA, (c) BMT and (d) IRT. For comparison, the TFs from Guzavina et al. (2019) with and without correcting tidal magnetic signal are also shown. The error bars indicate the uncertainties associated with the estimated TFs.

Figs. 9 present the selected elements of the estimated Q-matrix together with the corresponding squared coherency coefficients. For comparison, we also illustrate the dominant term (Q_{11}^{00}) estimated by Kuvshinov et al. (2021). Taking into account the uncertainties, the dominant term Q_{11}^{00} estimated via MagTFs once again shows a very close agreement with those estimated by Kuvshinov et al. (2021). Furthermore, the high squared coherency (> 0.9) underscores the robustness of the estimated dominant term Q_{11}^{00} is available. These results validate the reliability of estimating the Q-matrix from satellite data using MagTFs.

4. Conclusions

In this study, we have introduced a tool (named as MagTFs) designed to estimate multi-source magnetic TFs. These magnetic TFs are computed utilizing a reliable linear regression method with a section-averaged regression approach. The tool provides the capability to calculate magnetic TFs from signals originating from diverse sources. This encompasses MT tipplers, Sq global-to-local TFs from the ionosphere, and scalar C-response, along with Q-matrix from the magnetosphere. The tool is versatile, accommodating magnetic field measurements obtained from both land-based observatories and satellite-based observations.

To validate the functionality and practicality of MagTFs, four experiments were conducted to estimate magnetic TFs of ionospheric and magnetospheric origins. Geomagnetic signals measured at observatories and the Swarm satellites were used in these experiments. The effectiveness of MagTFs in processing both geomagnetic observatory and satellite data and accurately estimating multi-source magnetic TFs was confirmed by comparing the results with published findings. MagTFs is implemented in the C++ programming language and utilizes the OpenMP library to facilitate parallel computing. It is distributed as an open-source utility, ensuring accessibility and transparency in its use.

New features and functionalities can be extended for this tool in the future. For example, additional robust least-squares algorithms can be implemented to estimate the transfer functions. Second, we can correct the tidal magnetic signal to improve the accuracy of estimating Sq G2L TFs. Finally, the scalar C-response as applied to geomagnetic observatory data is based on the simplified Y_1^0 source assumption. Similar to the Sq G2L TFs, we can extend the tool to estimate G2L TFs for handling complex magnetospheric source structures (Püthe et al., 2015).

Code availability section

Name of the code: MagTFs

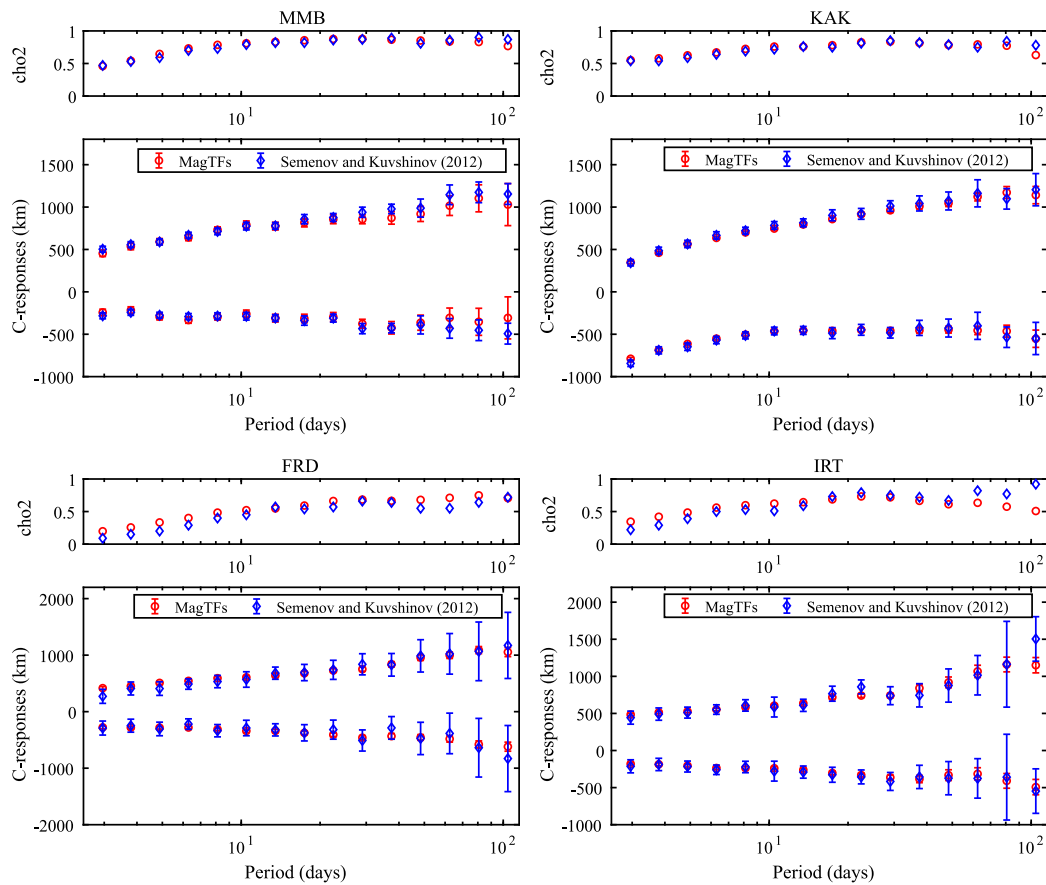


Fig. 7. Illustration of the estimated local scalar C-response by MagTFs and Semenov and Kuvshinov (2012) at four different observatories: (a) MMB, (b) KAK, (c) FRD, and (d) IRT. C-response in red are estimated by MagTFs, while C-response in blue is taken from Semenov and Kuvshinov (2012). Error bars indicate the uncertainties of the estimated C-response.

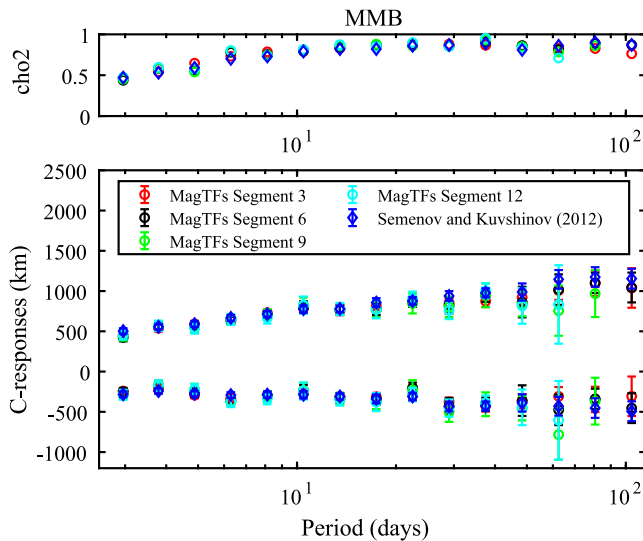


Fig. 8. Estimated C-responses at MMB observatory by Semenov and Kuvshinov (2012) and MagTFs with segment length of 3, 6, 9 and 12 units, respectively.

Hardware requirements: PC or server
 Program language: C++.
 Software required: Eigen.
 Program size: 26.0 MB

The developed MagTFs code and data from the four experiments are publicly available at Zenodo <https://doi.org/10.5281/zenodo.1079128> or GitHub (<https://github.com/hongbo-yao/MagTFs>).

CRediT authorship contribution statement

Zhengyong Ren: Writing – review & editing, Writing – original draft, Funding acquisition, Formal analysis, Conceptualization. **Zijun Zuo:** Writing – original draft, Visualization, Validation, Formal analysis. **Hongbo Yao:** Software, Methodology, Validation, Writing – original draft, Writing – review & editing. **Chaojian Chen:** Writing – original draft, Writing – review & editing, Methodology, Formal analysis. **Linan Xu:** Writing – review & editing, Formal analysis. **Jingtian Tang:** Writing – review & editing, Funding acquisition. **Keke Zhang:** Writing – review & editing, Funding acquisition.

Declaration of competing interest

The authors declare that they have no known competing financial interests or personal relationships that could have appeared to influence the work reported in this paper.

Acknowledgments

ZY, ZJ, CJ and JT are supported by grants from the National Natural Science Foundation of China (Grant Nos. 42250102, 42130810, 72088101), and the Science and Technology Innovation Program of Hunan Province (Grant No. 2021RC4055). HY and KZ are supported by the National Natural Science Foundation of China (42250101) and the Macao Foundation.

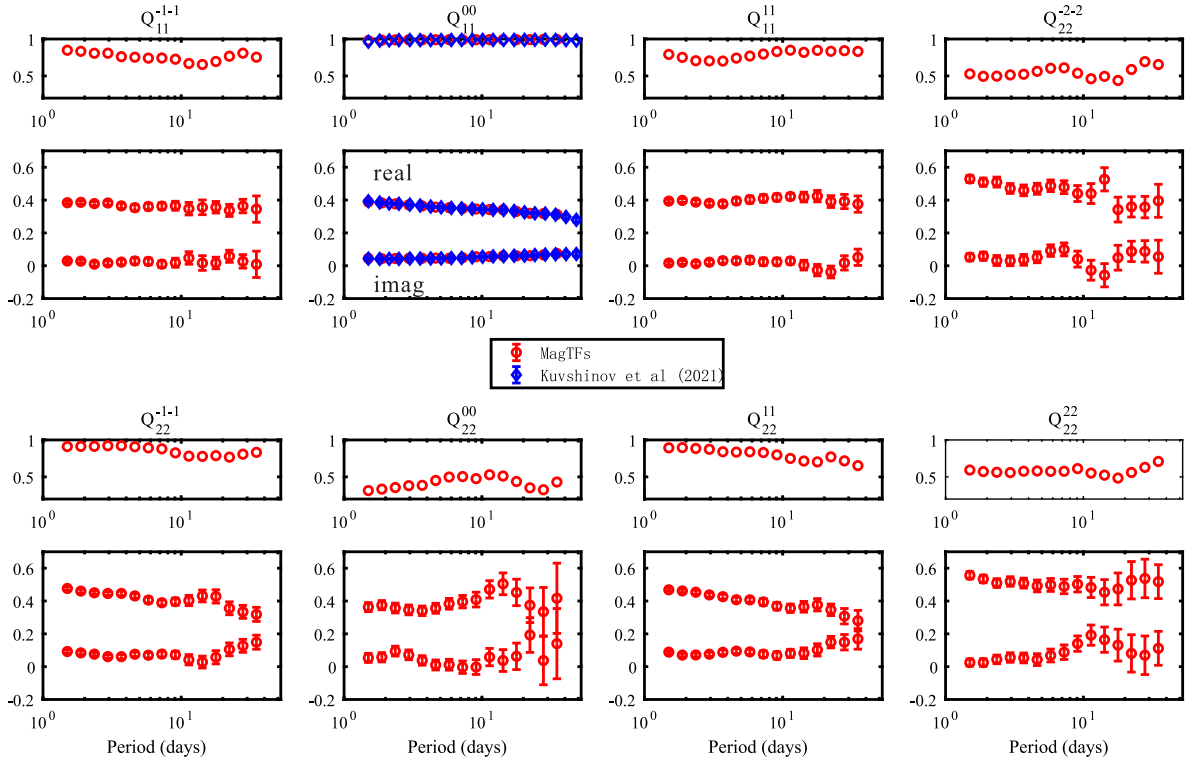


Fig. 9. Selected elements of Q-matrix and squared coherency coefficients estimated by MagTFs using satellite magnetic data, with error bars representing uncertainties. For comparison, the dominant Q_{11}^{00} term given by Kuvshinov et al. (2021) is also shown.

Appendix A. Procedure for estimating Sq global-to-local TFs

For a period of $T_p = 24$ hours ($p = 1$), Eq. (2) can be written as

$$Z(\mathbf{r}_s, \omega_p) = \sum_{m=0}^2 \sum_{n=m}^{m+3} \epsilon_n^m(\omega_p) T_n^m(\mathbf{r}_s, \omega_p) \\ = \epsilon_1^0(\omega_p) T_1^0(\mathbf{r}_s, \omega_p) + \epsilon_2^0(\omega_p) T_2^0(\mathbf{r}_s, \omega_p) + \dots + \epsilon_5^2(\omega_p) T_5^2(\mathbf{r}_s, \omega_p). \quad (15)$$

Therefore, the external source coefficients $\epsilon_n^m(\omega_p)$ are taken as input signals, while the vertical magnetic field component Z is the output signal. The procedure for estimating Sq global-to-local TFs at geomagnetic observatory \mathbf{r}_s and period $T_p = 24$ hours ($p = 1$) is as follows.

- (1) Estimate the spectra of the external source coefficients $\epsilon_n^m(\omega_p)$. First, we select all geomagnetically quiet days during the 1957–2022 interval. Second, for each quiet day i ($i = 1, 2, \dots, N_{Sq}$), we obtain the spectra of three magnetic field components of global geomagnetic observatories by Fourier transform. Finally, we estimate the spectra of the external source coefficients by fitting the magnetic field components using the potential method (Koch and Kuvshinov, 2013).
- (2) Assemble a least-squares system. For each observatory \mathbf{r}_s , the vertical magnetic field spectrum $Z(\mathbf{r}_s, \omega_k)$ and the external source coefficient $\epsilon_n^m(\omega_k)$ for N_{Sq} geomagnetic quiet-days are used to assemble the following least-squares system:

$$\begin{bmatrix} Z_1(\mathbf{r}_s, \omega_k) \\ Z_2(\mathbf{r}_s, \omega_k) \\ \vdots \\ Z_{N_{Sq}}(\mathbf{r}_s, \omega_k) \end{bmatrix} = \begin{bmatrix} \epsilon_{1,1}^0(\omega_k) & \epsilon_{2,1}^0(\omega_k) & \dots & \epsilon_{5,1}^2(\omega_k) \\ \epsilon_{1,2}^0(\omega_k) & \epsilon_{2,2}^0(\omega_k) & \dots & \epsilon_{5,2}^2(\omega_k) \\ \vdots & \vdots & \ddots & \vdots \\ \epsilon_{1,N_{Sq}}^0(\omega_k) & \epsilon_{2,N_{Sq}}^0(\omega_k) & \dots & \epsilon_{5,N_{Sq}}^2(\omega_k) \end{bmatrix} \begin{bmatrix} T_1^0(\mathbf{r}_s, \omega_k) \\ T_2^0(\mathbf{r}_s, \omega_k) \\ \vdots \\ T_5^2(\mathbf{r}_s, \omega_k) \end{bmatrix}. \quad (16)$$

- (3) Estimate TFs T_n^m by solving the above least-squares system with the IRLS algorithm and calculating standard errors using the method described in Section 2.2.

Appendix B. Procedure for estimating scalar C-response

As defined in Eq. (4), to estimate C-response, we first estimate the TFs $T(\mathbf{r}_s, \omega)$ defined by

$$T(\mathbf{r}_s, \omega) = \frac{B_r(\mathbf{r}_s, \omega)}{B_\theta(\mathbf{r}_s, \omega)}, \quad (17)$$

where the input signal is the time series of the colatitude magnetic field component B_θ , while the output signal is the time series of the radial magnetic field component B_r . The procedure for estimating C-response at geomagnetic observatory \mathbf{r}_s and period ω is as follows.

- (1) Obtain the spectra of the radial and colatitude magnetic field components $B_r(\mathbf{r}_s, \omega)$ and $B_\theta(\mathbf{r}_s, \omega)$ using steps (1)–(3) described in Section 2.2.
- (2) Assemble the following least-squares system:

$$\begin{bmatrix} B_r^{(1)}(\mathbf{r}_s, \omega) \\ B_r^{(2)}(\mathbf{r}_s, \omega) \\ \vdots \\ B_r^{(N)}(\mathbf{r}_s, \omega) \end{bmatrix} = \begin{bmatrix} B_\theta^{(1)}(\mathbf{r}_s, \omega) \\ B_\theta^{(2)}(\mathbf{r}_s, \omega) \\ \vdots \\ B_\theta^{(N)}(\mathbf{r}_s, \omega) \end{bmatrix} T(\mathbf{r}_s, \omega). \quad (18)$$

where N is the number of segments.

- (3) Estimate TFs $T(\mathbf{r}_s, \omega)$ by solving the above least-squares system with the IRLS algorithm and calculating standard errors using the method described in Section 2.2.
- (4) Convert $T(\mathbf{r}_s, \omega)$ to C-response by $C(\mathbf{r}_s, \omega) = -\frac{a \tan \theta}{2} T(\mathbf{r}_s, \omega)$.

Appendix C. Procedure for estimating Q-matrix

The Q-matrix as defined in Eq. (5) is a $N_{\text{ext}}(N_{\text{ext}} + 2) \times N_{\text{int}}(N_{\text{int}} + 2)$ matrix

$$\mathbf{Q} = \begin{bmatrix} Q_{11}^{-1-1} & Q_{11}^{0-1} & \cdots & Q_{N_{\text{int}}1}^{N_{\text{int}}-1} \\ Q_{11}^{-10} & Q_{11}^{00} & \cdots & Q_{N_{\text{int}}1}^{N_{\text{int}}0} \\ \vdots & \vdots & \ddots & \vdots \\ Q_{1N_{\text{ext}}}^{-1N_{\text{ext}}} & Q_{1N_{\text{ext}}}^{0N_{\text{ext}}} & \cdots & Q_{N_{\text{int}}N_{\text{ext}}}^{N_{\text{int}}N_{\text{ext}}} \end{bmatrix}. \quad (19)$$

where N_{ext} and N_{int} denote the maximum cutoff degrees describing the inducing ϵ_n^m and induced i_n^m spherical harmonic expansion coefficients (Kuvshinov et al., 2021). In practice, the Q-matrix is estimated column-by-column. The procedure for estimating each column of Q-matrix at period ω is as follows.

- (1) Obtain the spectra of the inducing and induced spherical harmonic coefficients $\epsilon_n^m(\omega)$ and $i_n^m(\omega)$ using steps (1)-(3) described in Section 2.2.
- (2) Assemble a least-squares system relating the inducing and induced spherical harmonic coefficients

$$\begin{bmatrix} \epsilon_{1,1}^{-1}(\omega) & \epsilon_{1,1}^0(\omega) & \cdots & \epsilon_{N_{\text{ext}},1}^{N_{\text{ext}}}(\omega) \\ \epsilon_{1,2}^{-1}(\omega) & \epsilon_{1,2}^0(\omega) & \cdots & \epsilon_{N_{\text{ext}},2}^{N_{\text{ext}}}(\omega) \\ \vdots & \vdots & \ddots & \vdots \\ \epsilon_{1,N}^{-1}(\omega) & \epsilon_{1,N}^0(\omega) & \cdots & \epsilon_{N_{\text{ext}},N}^{N_{\text{ext}}}(\omega) \end{bmatrix} \begin{bmatrix} Q_{k1}^{I-1}(\omega) \\ Q_{k1}^{I0}(\omega) \\ \vdots \\ Q_{kN}^{IN_{\text{ext}}}(\omega) \end{bmatrix} = \begin{bmatrix} i_{k,1}^I(\omega) \\ i_{k,2}^I(\omega) \\ \vdots \\ i_{k,N}^I(\omega) \end{bmatrix}. \quad (20)$$

- (3) Estimate one column of the Q-matrix by solving the above least-squares system with the IRLS algorithm and calculating standard errors using the method described in Section 2.2.

Repeating the above steps for different columns and periods, we can obtain all elements of the Q-matrix.

Data availability

Geomagnetic observatory data are available from the British Geological Survey via https://imag-data.bgs.ac.uk/GIN_V1/GINForms2. Swarm satellite data are available from <https://earth.esa.int/eogateway/missions/swarm/data>.

References

- Arranz, C.J., Marchese, V., Léger, J.-M., Vallmitjana, M., Jager, T., Pous, M., 2023. Magnetic cleanliness on NanoMagSat, a CubeSats' constellation science mission. In: 2023 International Symposium on Electromagnetic Compatibility – EMC Europe. pp. 1–6. <http://dx.doi.org/10.1109/EMCEurope57790.2023.10274205>.
- Aster, R.C., Borchers, B., Thurber, C.H., 2018. Parameter Estimation and Inverse Problems. Elsevier, Amsterdam, Netherlands. <http://dx.doi.org/10.1016/C2015-0-02458-3>.
- Baba, K., Chave, A.D., Evans, R.L., Hirth, G., Mackie, R.L., 2006. Mantle dynamics beneath the east Pacific rise at 17°S: Insights from the mantle electromagnetic and tomography (MELT) experiment. *J. Geophys. Res. Solid Earth* 111 (B2), <http://dx.doi.org/10.1029/2004JB003598>.
- Bahr, K., Filloux, J.H., 1989. Local sq response functions from EMSLAB data. *J. Geophys. Res. Solid Earth* 94 (B10), 14195–14200. <http://dx.doi.org/10.1029/JB094iB10p14195>.
- Balas, G., Egbert, G., 2006. Empirical orthogonal function analysis of magnetic observatory data: Further evidence for non-axisymmetric magnetospheric sources for satellite induction studies. *Geophys. Res. Lett.* 33, <http://dx.doi.org/10.1029/2006GL025721>.
- Banks, R., 1969. Geomagnetic variations and the electrical conductivity of the upper mantle. *Geophys. J. R. Astron. Soc.* 17, 457–487. <http://dx.doi.org/10.1111/j.1365-246X.1969.tb00252.x>.

- Berdichevsky, M.N., Dmitriev, V.I., 2008. Models and Methods of Magnetotellurics. Springer Science & Business Media, <http://dx.doi.org/10.1007/978-3-540-77814-1>.
- Chave, A., Jones, A., 2012. The Magnetotelluric Method. Theory and Practice. Cambridge University Press, New York, <http://dx.doi.org/10.1017/CBO9781139020138>.
- Chave, A.D., Thomson, D.J., 1989. Some comments on magnetotelluric response function estimation. *J. Geophys. Res.* 94 (B10), 14215–14225. <http://dx.doi.org/10.1029/jb094ib10p14215>.
- Chave, A.D., Thomson, D.J., 2003. A bounded influence regression estimator based on the statistics of the hat matrix. *J. R. Stat. Soc. Ser. C. Appl. Stat.* 52 (3), 307–322. <http://dx.doi.org/10.1111/1467-9876.00406>.
- Chen, C., Kruglyakov, M., Kuvshinov, A., 2020. A new method for accurate and efficient modeling of the local ocean induction effects. Application to long-period responses from island geomagnetic observatories. *Geophys. Res. Lett.* 47 (8), e2019GL086351. <http://dx.doi.org/10.1029/2019GL086351>.
- Chen, C., Kuvshinov, A., Kruglyakov, M., Munch, F., Rigaud, R., 2023. Constraining the crustal and mantle conductivity structures beneath islands by a joint inversion of multi-source magnetic transfer functions. *J. Geophys. Res. Solid Earth* 128 (1), e2022JB024106. <http://dx.doi.org/10.1029/2022JB024106>.
- Fuentes-Arreazola, M.A., Núñez, D., Núñez-Cornú, F.J., Calderón-Moctezuma, A., Ruiz-Aguilar, D., Romo-Jones, J.M., 2021. Magnetotelluric imaging of the ceboruco volcano, nayarit, Mexico. *J. Volcanol. Geotherm. Res.* 418, 107339. <http://dx.doi.org/10.1016/j.jvolgeores.2021.107339>.
- Grayver, A., 2024. Unravelling the electrical conductivity of earth and planets. *Surv. Geophys.* 1–52. <http://dx.doi.org/10.1007/s10712-023-09813-9>.
- Gresse, M., Uyeshima, M., Koyama, T., Hase, H., Aizawa, K., Yamaya, Y., Morita, Y., Weller, D., Rung-Arunwan, T., Kaneko, T., et al., 2021. Hydrothermal and magmatic system of a volcanic island inferred from magnetotellurics, seismicity, self-potential, and thermal image: an example of Miyakejima (Japan). *J. Geophys. Res. Solid Earth* 126 (6), e2021JB022034. <http://dx.doi.org/10.1029/2021JB022034>.
- Guzavina, M., Grayver, A., Kuvshinov, A., 2018. Do ocean tidal signals influence recovery of solar quiet variations? *Earth Planets Space* 70, <http://dx.doi.org/10.1186/s40623-017-0769-1>.
- Guzavina, M., Grayver, A., Kuvshinov, A., 2019. Probing upper mantle electrical conductivity with daily magnetic variations using global to local transfer functions. *Geophys. J. Int.* 219 (3), 2125–2147. <http://dx.doi.org/10.1093/gji/ggz412>.
- Karato, S.-i., Wang, D., 2013. Electrical conductivity of minerals and rocks. *Chem. Deep Earth* 145–182. <http://dx.doi.org/10.1002/9781118529492.ch5>.
- Kelbert, A., Schultz, A., Egbert, G., 2009. Global electromagnetic induction constraints on transition-zone water content variations. *Nature* 460, 1003–1007. <http://dx.doi.org/10.1038/nature08257>.
- Kerridge, D., 2001. INTERMAGNET: Worldwide near-real-time geomagnetic observatory data. In: Proceedings of the Workshop on Space Weather. vol. 34, ESTEC, URL: https://intermagnet.org/docs/publications/IM_ESTEC.pdf.
- Koch, S., Kuvshinov, A., 2013. Global 3-D EM inversion of sq variations based on simultaneous source and conductivity determination. A concept and its validation. *Geophys. J. Int.* <http://dx.doi.org/10.1093/gji/ggt227>.
- Kuvshinov, A., 2012. Deep electromagnetic studies from land, sea, and space: progress status in the past 10 years. *Surv. Geophys.* 33 (1), 169–209. <http://dx.doi.org/10.1007/s10712-011-9118-2>.
- Kuvshinov, A., Grayver, A., Toffner Clausen, L., Olsen, N., 2021. Probing 3-D electrical conductivity of the mantle using 6 years of Swarm, CryoSat-2 and observatory magnetic data and exploiting matrix Q-responses approach. *Earth Planets Space* 73 (1), 1–26. <http://dx.doi.org/10.1186/s40623-020-01341-9>.
- Li, S., Weng, A., Zhang, Y., Schultz, A., Li, Y., Tang, Y., Zou, Z., Zhou, Z., 2020. Evidence of bermuda hot and wet upwelling from novel three-dimensional global mantle electrical conductivity image. *Geochem. Geophys. Geosyst.* 21 (6), e2020GC009016.
- Li, G., Zhou, X., Chen, C., Xu, L., Zhou, F., Shi, F., Tang, J., 2023. Multi-type geomagnetic noise removal via an improved U-Net deep learning network. *IEEE Trans. Geosci. Remote Sens.* <http://dx.doi.org/10.1109/TGRS.2023.3307422>.
- Luhr, H., Xiong, C., Olsen, N., 2017. Near-earth magnetic field effects of large-scale magnetospheric currents. *Space Sci. Rev.* 206, 521–545. <http://dx.doi.org/10.1016/j.srt.2018.11.017>.
- Morschhauser, A., Grayver, A., Kuvshinov, A., Samrock, F., Matzka, J., 2019. Tippers at island geomagnetic observatories constrain electrical conductivity of oceanic lithosphere and upper mantle. *Earth Planets Space* 71 (1), 1–9. <http://dx.doi.org/10.1186/s40623-019-0991-0>.
- Munch, F.D., Grayver, A.V., Guzavina, M., Kuvshinov, A.V., Khan, A., 2020. Joint inversion of daily and long-period geomagnetic transfer functions reveals lateral variations in mantle water content. *Geophys. Res. Lett.* 47 (10), e2020GL087222. <http://dx.doi.org/10.1029/2020GL087222>.
- Munch, F., Grayver, A., Kuvshinov, A., Khan, A., 2018. Stochastic inversion of geomagnetic observatory data including rigorous treatment of the ocean induction effect with implications for transition zone water content and thermal structure. *J. Geophys. Res.* 123, 31–51. <http://dx.doi.org/10.1002/2017JB014691>.
- Murphy, B.S., Lucas, G.M., Love, J.J., Kelbert, A., Bedrosian, P.A., Rigler, E.J., 2021. Magnetotelluric sampling and geoelectric hazard estimation: Are national-scale surveys sufficient? *AGU Space Weather* 19 (7), <http://dx.doi.org/10.1029/2020SW002693>.

- Olsen, N., 1998. The electrical conductivity of the mantle beneath Europe derived from C-responses from 3 to 720 hr. *Geophys. J. Int.* 133 (2), 298–308. <http://dx.doi.org/10.1046/j.1365-246X.1998.00503.x>.
- Olsen, N., 1999a. Induction studies with satellite data. *Surv. Geophys.* 20, 309–340. <http://dx.doi.org/10.1023/A:1006611303582>.
- Olsen, N., 1999b. Long-period (30 days–1 year) electromagnetic sounding and the electrical conductivity of the lower mantle beneath Europe. *Geophys. J. Int.* 138, 179–187. <http://dx.doi.org/10.1046/j.1365-246X.1999.00854.x>.
- Olsen, N., Albin, G., Bouffard, J., Parrinello, T., Tøffner Clausen, L., 2020. Magnetic observations from CryoSat-2: calibration and processing of satellite platform magnetometer data. *Earth Planets Space* 72, 1–18. <http://dx.doi.org/10.1186/s40623-020-01171-9>.
- Olsen, N., Friis-Christensen, E., Floberghagen, R., 2013. The *Swarm* satellite constellation application and research facility (SCARF) and *Swarm* data products. *Earth Planets Space* 65, 1189–1200. <http://dx.doi.org/10.5047/eps.2013.07.001>.
- Püthe, C., 2015. Interpretation of Global EM Induction Data from Ground, Sea and Space: New Response Functions, Inversion Schemes and Conductivity Models (Ph.D. thesis). ETH Zurich, URL: <https://api.semanticscholar.org/CorpusID:62834072>.
- Püthe, C., Kuvshinov, A., 2014. Mapping 3-D mantle electrical conductivity from space: a new 3-D inversion scheme based on analysis of matrix Q-responses. *Geophys. J. Int.* 197 (2), 768–784.
- Püthe, C., Kuvshinov, A., Olsen, N., 2015. Handling complex source structures in global EM induction studies: from C-responses to new arrays of transfer functions. *Geophys. J. Int.* 201 (1), 318–328. <http://dx.doi.org/10.1093/gji/ggv021>.
- Reigber, C., Lühr, H., Schwintzer, P., 2002. CHAMP mission status. *Adv. Space Res.* 30 (2), 129–134. [http://dx.doi.org/10.1016/S0273-1177\(02\)00276-4](http://dx.doi.org/10.1016/S0273-1177(02)00276-4).
- Rigaud, R., Kuvshinov, M., Kuvshinov, A., Pinheiro, K., Petereit, J., Matzka, J., Marshalko, E., 2021. Exploring effects in tippers at island geomagnetic observatories due to realistic depth- and time-varying oceanic electrical conductivity. *Earth Planets Space* 73 (3), <http://dx.doi.org/10.1186/s40623-020-01339-3>.
- Sabaka, T.J., Tøffner Clausen, L., Olsen, N., Finlay, C.C., 2018. A comprehensive model of Earth's magnetic field determined from 4 years of *Swarm* satellite observations. *Earth Planets Space* 70 (1), 1–26. <http://dx.doi.org/10.1186/s40623-018-0896-3>.
- Sabaka, T.J., Olsen, N., Purucker, M.E., 2004. Extending comprehensive models of the Earth's magnetic field with Ørsted and CHAMP data. *Geophys. J. Int.* 159 (2), 521–547. <http://dx.doi.org/10.1111/j.1365-246X.2004.02421.x>.
- Schmucker, U., 1970. Anomalies of Geomagnetic Variations in the South-Western United States. vol. 13, *Bull. Scripps Inst. Ocean, Univ. Calif.*, URL: <https://api.semanticscholar.org/CorpusID:129307038>.
- Schmucker, U., 1999a. A spherical harmonic analysis of solar daily variations in the years 1964–65 – I. Methods. *Geophys. J. Int.* 136, 439–454. <http://dx.doi.org/10.1046/j.1365-246X.1999.00742.x>.
- Schmucker, U., 1999b. A spherical harmonic analysis of solar daily variations in the years 1964–1965: response estimates and source fields for global induction-II. results. *Geophys. J. Int.* 136, 455–476. <http://dx.doi.org/10.1046/j.1365-246X.1999.00743.x>.
- Schultz, A., Larsen, J.C., 1987. On the electrical conductivity of the mid-mantle – I. Calculation of equivalent scalar magnetotelluric response functions. *Geophys. J. R. Astron. Soc.* 88, 733–761. <http://dx.doi.org/10.1111/j.1365-246X.1987.tb01654.x>.
- Semenov, A., Kuvshinov, A., 2012. Global 3-D imaging of mantle conductivity based on inversion of observatory C-responses-II. Data analysis and results. *Geophys. J. Int.* 191 (3), 965–992. <http://dx.doi.org/10.1111/j.1365-246X.2012.05665.x>.
- Shao, Q., Liu, Y., Luo, Y., Heinson, G., Xu, Y., Du, J., Chen, C., 2024. Geoelectric field estimations during geomagnetic storm in North China from SinoProbe magnetotelluric impedances. *Space Weather* 22 (4), e2023SW003758. <http://dx.doi.org/10.1029/2023SW003758>.
- Wood, A.G., Alfonsi, L., Clausen, L.B., Jin, Y., Spogli, L., Urbář, J., Rawlings, J.T., Whittaker, I.C., Dorrian, G.D., Høeg, P., et al., 2022. Variability of ionospheric plasma: results from the ESA swarm mission. *Space Sci. Rev.* 218 (6), 52. <http://dx.doi.org/10.1007/s11214-022-00916-0>.
- Yamazaki, Y., Maute, A., 2017. Sq and EEJ—A review on the daily variation of the geomagnetic field caused by ionospheric dynamo currents. *Space Sci. Rev.* 206 (1–4), 299–405, URL: <http://dx.doi.org/10.1007/s11214-016-0282-z>.
- Yan, Q., Yao, H., 2024. Recent geomagnetic storms observed by Macau Science Satellite-1. *Earth Planet. Phys.* 8 (4), 565–569. <http://dx.doi.org/10.26464/epp2024047>.
- Yao, H., Ren, Z., Pan, K., Tang, J., Zhang, K., 2023a. A global mantle conductivity model derived from 8 years of *Swarm* satellite magnetic data. *Earth Planet. Phys.* 7 (1), 49–56. <http://dx.doi.org/10.26464/EPP2023011>.
- Yao, H., Ren, Z., Tang, J., Guo, R., Yan, J., 2023b. Trans-dimensional Bayesian joint inversion of magnetotelluric and geomagnetic depth sounding responses to constrain mantle electrical discontinuities. *Geophys. J. Int.* 233 (3), 1821–1846. <http://dx.doi.org/10.1093/gji/ggad029>.
- Yao, H., Ren, Z., Tang, J., Zhang, K., 2022. A multi-resolution finite-element approach for global electromagnetic induction modeling with application to southeast China coastal geomagnetic observatory studies. *J. Geophys. Res. Solid Earth* 127 (8), e2022JB024659. <http://dx.doi.org/10.1029/2022JB024659>.
- Yoshino, T., Katsura, T., 2013. Electrical conductivity of mantle minerals: role of water in conductivity anomalies. *Annu. Rev. Earth Planet. Sci.* 41, 605–628. <http://dx.doi.org/10.1146/annurev-earth-050212-124022>.
- Yuan, Y., Uyeshima, M., Huang, Q., Tang, J., Li, Q., Teng, Y., 2020. Continental-scale deep electrical resistivity structure beneath China. *Tectonophysics* 790, 228559. <http://dx.doi.org/10.1016/j.tecto.2020.228559>.
- Zhang, K., 2023. A novel geomagnetic satellite constellation: science and applications. *Earth Planet. Phys.* 7 (1), 4–21. <http://dx.doi.org/10.26464/epp2023019>.
- Zhang, H., Egbert, G., Huang, Q., 2023. Constraints on MTZ water content from joint inversion of diurnal variations and magnetospheric signals. *Geophys. Res. Lett.* 50 (10), e2023GL102765. <http://dx.doi.org/10.1029/2023GL102765>.
- Zhang, Y., Weng, A., Li, S., Yang, Y., Tang, Y., Liu, Y., 2020. Electrical conductivity in the mantle transition zone beneath Eastern China derived from L1-Norm C-responses. *Geophys. J. Int.* 221 (2), 1110–1124. <http://dx.doi.org/10.1093/gji/ggaa059>.
- Zhao, G., Zhang, X., Cai, J., Zhan, Y., Ma, Q., Tang, J., Du, X., Han, B., Wang, L., Chen, X., et al., 2022. A review of seismo-electromagnetic research in China. *Sci. China Earth Sci.* 65 (7), 1229–1246. <http://dx.doi.org/10.1007/s11430-021-9930-5>.